Magnetic resonance monitoring of focused ultrasound/magnetic nanoparticle targeting delivery of therapeutic agents to the brain

Hao-Li Liu[a,b,1], Mu-Yi Hua[c,1], Hung-Wei Yang[c,1], Chiung-Yin Huang[d], Po-Chun Chu[a], Jia-Shin Wu[a], I-Chou Tseng[d], Jiun-Jie Wang[e], Tzu-Chen Yen[b,f], Pin-Yuan Chen[d,g,2,3], and Kuo-Chen Wei[d,2,3]

Departments of [a]Electrical Engineering, [c]Chemical and Material Engineering, and [e]Medical Image and Radiological Sciences and [g]Graduate Institute of Clinical Medical Sciences, Chang-Gung University, Taoyuan 333, Taiwan; [b]Molecular Imaging Center and [f]Department of Nuclear Medicine, Chang-Gung Memorial Hospital, Taoyuan 333, Taiwan; and [d]Department of Neurosurgery, Chang-Gung University College of Medicine and Memorial Hospital, Taoyuan 333, Taiwan

Edited by Ralph Weissleider, Harvard Medical School, Boston, MA, and accepted by the Editorial Board July 13, 2010 (received for review March 16, 2010)

The superparamagnetic properties of magnetic nanoparticles (MNPs) allow them to be guided by an externally positioned magnet and also provide contrast for MRI. However, their therapeutic use in treating CNS pathologies in vivo is limited by insufficient local accumulation and retention resulting from their inability to traverse biological barriers. The combined use of focused ultrasound and magnetic targeting synergistically delivers therapeutic MNPs across the blood–brain barrier to enter the brain both passively and actively. Therapeutic MNPs were characterized and evaluated both in vitro and in vivo, and MRI was used to monitor and quantify their distribution in vivo. The technique could be used in normal brains or in those with tumors, and significantly increased the deposition of therapeutic MNPs in brains with intact or compromised blood–brain barriers. Synergistic targeting and image monitoring are powerful techniques for the delivery of macromolecular chemotherapeutic agents into the CNS under the guidance of MRI.

blood–brain barrier | brain drug delivery | focused ultrasound | magnetic nanoparticles | magnetic targeting

Within the CNS, the blood–brain barrier (BBB) excludes larger (>400 Da) molecules from entering the brain parenchyma, protecting it from toxic foreign substances (1). However, it also prohibits delivery of many potentially effective diagnostic or therapeutic agents and restricts the enhanced permeability and retention (EPR) of therapeutic nanoparticles. Many factors affect EPR, including the pH, polarity, and size of the delivered substance. Even when pathologic processes compromise the integrity or function of the BBB, EPR can be limited by microenvironmental characteristics such as hypovascularity, fibrosis, or necrosis (2–4).

In the presence of microbubbles and with use of a low-energy burst tone, focused ultrasound (FUS) can increase the permeability of the BBB (5). This noninvasive procedure disrupts the BBB locally rather than systemically, minimizing off-target effects. Furthermore, the disruption is reversible within several hours, providing a window of opportunity to achieve local delivery of chemotherapeutic agents in brains with intact or compromised BBBs. However, drug delivery in such cases is passive, relying on the free diffusion of the agents across the barrier.

Advances in nanotechnology and molecular biology have allowed development of novel nanomedical platforms (6–8). Such approaches allow simultaneous diagnostic imaging and drug delivery monitoring in vivo in real time (9, 10). Magnetic nanoparticles (MNPs) have intrinsic magnetic properties that enable their use as contrast agents in MRI (8, 11). Because MNPs are also sensitive to external magnetic forces, magnetic targeting (MT) actively enhances their deposition at the target site, increasing the therapeutic dose delivered beyond that obtainable by passive diffusion (12).

This study combines FUS and MT of nanoparticles as a synergistic delivery system for chemotherapeutic agents concurrent with MRI monitoring for treating CNS diseases. FUS creates the opportunity to deliver therapeutic MNPs by passive local EPR, and externally applied magnetic forces actively increase the local MNP concentration. When combined, these techniques permit the delivery of large molecules into the brain (Fig. 1). Furthermore, the deposition of the therapeutic MNPs can be monitored and quantified in vivo by MRI.

Results

Characterization of Therapeutic MNPs. The saturated magnetization, mean hydrodynamic size, and particle size of the commercially available MNP Resovist and the newly synthesized MNPs generated for this study are summarized in Table S1. As measured by transmission EM (TEM), MNP-3 had a mean diameter of 12.3 nm (Fig. 2*A*). This was significantly smaller than the hydrodynamic sizes measured by dynamic light scattering (64 nm for Resovist, 74–83 nm for MNPs-1–3; Fig. S1*A* and Table S1), although such differences could be attributable to solvent effects. The measured zeta potentials of all of the synthesized MNPs were similar to that of Resovist (approximately 45 mV).

Magnetization of MNPs is crucial for their utility in MT, and crystallinity significantly affects this parameter. During synthesis, the crystallinity of the MNPs was manipulated by controlling the reaction conditions. MNP-3 exhibited the best crystallinity among the MNPs tested (Fig. S1*C*) and also displayed the highest degree of magnetization (Fig. S1*B*).

Administration of the MNPs into biological tissues profoundly alters the spin–spin relaxation rate (R2), and thus can serve as an indicator of the MRI contrast agent. The R2, and hence the detection sensitivity, of MNP-3 was twice that of Resovist by MRI (Fig. 2 *E* and *F* and Table S1).

The polymer poly[aniline-*co*-*N*-(1-one-butyric acid)] aniline (SPAnH) was used to encapsulate iron oxide (Fe_3O_4). This process decreases the aggregation typical of MNPs and improves their stability in aqueous solutions. Fourier transform IR (FT-IR) spectroscopy indicated that the surface of the Fe_3O_4 particles was covered with a layer of the SPAnH polymer, and that the out-

Author contributions: H.-L.L., M.-Y.H., H.-W.Y., P.-Y.C., and K.-C.W. designed research; H.-L.L., M.-Y.H., H.-W.Y., C.-Y.H., P.-C.C., J.-S.W., I.-C.T., J.-J.W., T.-C.Y., and P.-Y.C. performed research; H.-L.L., M.-Y.H., and H.-W.Y. contributed new reagents/analytic tools; H.-L.L., M.-Y.H., H.-W.Y., C.-Y.H., P.-C.C., J.-S.W., I.-C.T., J.-J.W., T.-C.Y., P.-Y.C., and K.-C.W. analyzed data; and H.-L.L., M.-Y.H., H.-W.Y., and K.-C.W. wrote the paper.

The authors declare no conflict of interest.

This article is a PNAS Direct Submission. R.W. is a guest editor invited by the Editorial Board.

Freely available online through the PNAS open access option.

[1]H.-L.L., M.-Y.H., and H.-W.Y. contributed equally to this work.

[2]P.-Y.C. and K.-C.W. contributed equally to this work.

[3]To whom correspondence may be addressed. E-mail: kuochenwei@adm.cgmh.org.tw or pinyuanc@adm.cgmh.org.tw.

This article contains supporting information online at www.pnas.org/lookup/suppl/doi:10.1073/pnas.1003388107/-/DCSupplemental.

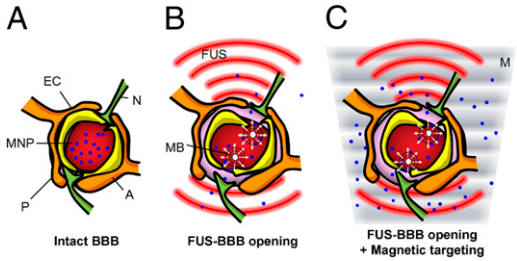

Fig. 1. Schematic of treatment protocol. (*A*) Intact CNS capillaries block MNP delivery into the brain parenchyma. (*B*) In the presence of microbubbles (MB), FUS temporarily disrupts the BBB, enhancing passive influx of therapeutic MNPs at the target location. (*C*) Combining MT (M) with FUS actively targets the therapeutic MNPs to the brain. (A, astrocyte; EC, endothelial cell; N, neuron; P, pericyte.)

ermost layer of the composite maintained the –NH and –COOH groups, which could be used to immobilize drugs or other biomaterials (Fig. 2*D*).

Epirubicin is a cytotoxic anticancer agent used to treat malignant tumors. It is similar in structure to doxorubicin (except for a hydroxyl group at the 4′ position of the daunosamine sugar), but has less myocardial and nerve cell toxicity than doxorubicin (13). When epirubicin was immobilized on the surface of the MNPs, the particles exhibited four new peaks attributable to the drug (Fig. 2*D*). The orange fluorescence emitted by epirubicin in confocal microscopy confirmed that the drug colocalized with the MNPs (Fig. 2*B*).

MNPs can become saturated with epirubicin because they have a fixed number of carboxyl groups on their surface. To decrease the quantity of MNPs required for effective treatment, epirubicin must be immobilized on their surface at therapeutically effective levels. HPLC analysis showed that, in this synthesis, epirubicin immobilization maximized at 300.294 μg of epirubicin bound per 1 mg of MNP (Fig. 2*C*), equivalent to 452 μg of epirubicin per 1 mg of iron ion.

Aggregation of MNPs in Vitro. The ability of MNPs to be attracted by an external magnetic field was tested in vitro. Resovist failed to aggregate when it was infused through plastic tubing at a constant flow rate and at a fixed distance from an external applied magnetic field. In contrast, under the same conditions, significant accumulation of MNP-3 was observed (Fig. S2 *A–D*). An approximate doubling of the medium viscosity led to a nearly 50% decrease in MNP aggregation, suggesting that the efficiency of MT is inversely proportional to viscous drag (Fig. S2*E*).

Cell Toxicity of Therapeutic MNPs in Vitro. MNPs without conjugated epirubicin had no apparent cytotoxic effect when cocultured in vitro with tumor cells (Fig. S3*E*). In contrast, numerous epirubicin-MNPs, presumably taken up by endocytosis, were visible within the cells by TEM (Fig. S3*G*; confirmed by diffraction patterns in Fig. S3*H*). Furthermore, the particles passed into the nuclei and appear to have induced apoptosis. Conjugating epirubicin to the MNPs did not affect the drug's cytotoxicity: the IC_{50} of free epirubicin and epirubicin-MNPs were 6.7 μg/mL and 5.2 μg/mL, respectively. The IC_{50} was reduced significantly to 1.7 μg/mL when MT was applied (Fig. S3*F*). The effects of MT on epirubicin-MNPs was confirmed by fluorescence microscopy: The number of live cells (green) decreased as the dose of epirubicin-MNPs increased, and tumor cell toxicity was concentrated at the site where the magnet was positioned (Fig. S3 *A–D*).

MRI Contrast Enhancement and MNP Quantification in Vivo. The enhancement of local MNP delivery into brain via combined FUS and MT was evaluated. Contrast-enhanced T1-weighted images confirmed that FUS disrupted the BBB (Figs. S4 and S5). R2 maps (showing changes caused by different amounts of MNP) and T2* imaging (indicating susceptibility artifact–induced signal loss caused by MNP accumulation) showed that FUS treatment alone increased local deposition of MNP-3 by 21.5% relative to the contralateral hemisphere (Fig. 3). Subsequently applying MT increased MNP accumulation, with a 6-h exposure causing the greatest increase in MNP concentration (244.6% relative to the

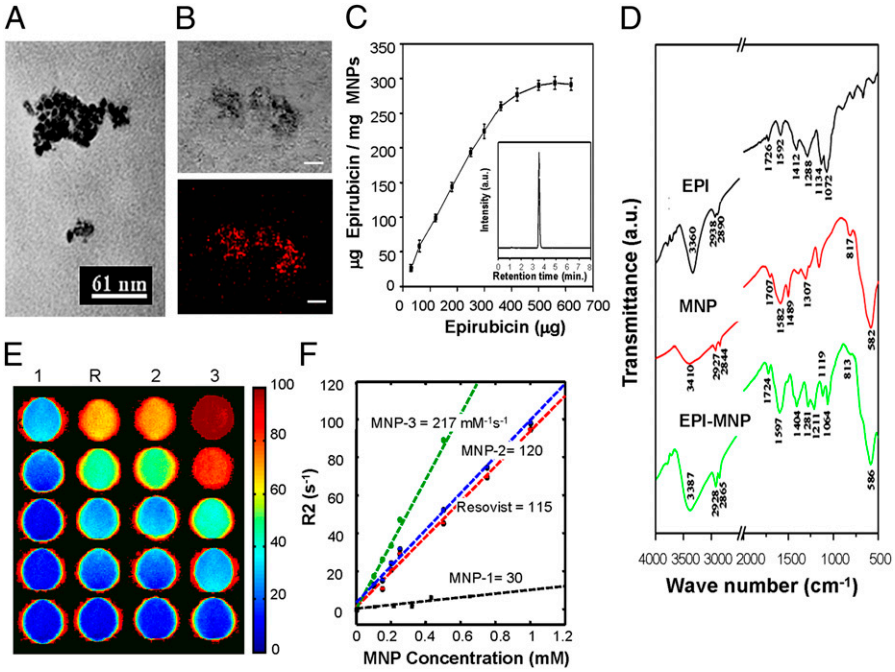

Fig. 2. Characterization of MNPs. (*A*) TEM image of MNP-3. (*B*) Phase (*Upper*) and fluorescence (*Lower*) confocal microscopy show epirubicin immobilized on MNPs. (Scale bar: 10 μm.) (*C*) HPLC quantification of epirubicin immobilized on 1 mg of MNP-3 versus added epirubicin. Values are means ± SD ($n = 6$). (*D*) FT-IR spectra of epirubicin, MNP-3, and epirubicin-MNP-3. The four peaks characteristic of epirubicin (1,724 cm^{-1}, 1,404 cm^{-1}, 1,119 cm^{-1}, 1,064 cm^{-1}) indicate immobilization of the drug on the MNP surface. (*E*) Spin-spin relaxivities (R2) of Resovist (R) and MNP-1–3. (*F*) Concentration dependence of MNP relaxivities.

contralateral hemisphere) but also a wider distribution (as seen in T2* imaging) relative to brains treated with FUS alone (Fig. 3). The combination of FUS and 6 h of MT deposited 21,738 ± 3,477 ng of epirubicin per gram of brain tissue, whereas treatment with FUS alone accumulated only 1,336 ± 1,182 ng epirubicin per gram of tissue. Furthermore, local MNP capture was dependent on field strength: a 0.55-T magnet attracted four times more MNPs than a 0.18-T magnet, as assessed by R2 mapping (Fig. S6 *C* and *D*).

The amount of MNPs accumulated in brain parenchyma was also measured by inductively coupled plasma optical emission spectrometry (ICP-OES) and the epirubicin concentration was measured by HPLC (Fig. 4). Neither FUS alone nor MT alone caused significant MNP accumulation in the experimental brain site. Furthermore, accumulation was no more significant on the experimental side relative to the contralateral side with either of these treatments. However, when FUS and MT were combined, MNP accumulation increased dramatically, with MNP-3 showing the highest levels of accumulation. Furthermore, the accumulation was markedly more pronounced on the side subjected to MT. Interestingly, when MNP-2 was used, the ratio of MNP accumulation between the experimental and contralateral hemispheres reached a maximum at 6 h but decreased quickly at 12 h of MT, whereas the ratio was maintained when MNP-3 was administered. This suggests that MNPs with higher R2 values can contribute a higher magnetic moment (thus enhancing MT and maintaining localized epirubicin concentrations at therapeutic levels) and are less likely to be cleared from the bloodstream as foreign bodies than those with lower R2 values. Most importantly, this ratio correlated highly ($r^2 = 0.908$) with the values measured in vivo using R2 maps, indicating that such maps provide a good estimation of MNP (and thus drug) localization and concentration in vivo (Fig. 4*D*). Based on comparisons between the ICP-OES/HPLC analyses and the R2 relaxivities determined by MRI, 1 mM (or 4×10^{-3} mmol) of MNP-3 detected on R2 maps was equivalent to an epirubicin concentration of 133,894 ng/g of tissue, or 617 ng/g of epirubicin per change in R2 (in s^{-1}). MNP deposition in the brain was confirmed histologically by Prussian blue staining of iron deposits (Fig. S5 *E* and *F*).

Enhancement of Therapeutic MNP Delivery to Brain Tumors. Tumor-bearing animals were treated with epirubicin-MNP without (control) or with combined FUS/MT treatment. Control animals showed no MNP accumulation in the tumor region 6 h after epirubicin-MNP administration (Fig. 5*A*). However, relaxation rates increased 2.6-fold (to 35.8 ± 5.2 s^{-1} relative to control values of 13.6 ± 4.5 s^{-1}) at the tumor site by applying MT for 6 h after FUS treatment (Fig. 5 *B* and *C*). After correcting for the baseline value contributed by blood circulation, it was estimated that 0.16 ± 0.03 mM of MNPs was delivered to the tumor, equivalent to 11,982 ± 2,105 ng of epirubicin per gram of tissue. This is approximately 15-fold higher than the therapeutic range (819 ± 482 ng/g tumor) reported for in vivo doxorubicin, which has a clinical response rate of 39% in patients with breast carcinoma (17). Furthermore, TEM showed that FUS apparently induced interendothelial clefts with no obvious tight-junctional complexes in tumors (Fig. 5*D*), and that epirubicin-MNPs were taken up by tumor cells and macrophages (Fig. 5 *E* and *F*). In contrast, MNP injection alone caused no ischemic or histological changes in the brain during the period studied. Confocal and fluorescence microscopy (Fig. 5 *G* and *H* and Fig. S7 *C* and *H*) and Prussian blue staining (Fig. S7 *B* and *G*) confirmed that more epirubicin-MNPs were deposited at the tumor site than in the contralateral side. Thus, epirubicin localization was enhanced significantly within the brain parenchyma by FUS/MT, whereas it appeared in only the capillary bed in the contralateral hemisphere, indicating that off-target effects were minimal. Furthermore, the correlation between MNP distribution (as determined by Prussian blue staining) and epirubicin fluorescence confirmed that MNPs are effective carriers for epirubicin, and by extension, that MRI R2 mapping can be used to detect localized concentrations of the drug with a high degree of precision.

Experimental treatment of animals with induced tumors showed that combining therapeutic MNPs with FUS/MT provided the most effective means of controlling tumor progression: over a 7-d period, tumor volume increased only 106 ± 24% in treated animals, compared with a 313% increase (±103%) in controls. Furthermore, although treatment with therapeutic MNPs alone or epirubicin-MNP with FUS improved median animal survival to only 23 and 20 d, respectively, survival improved significantly in animals receiving epirubicin-MNPs in conjunction with FUS/MT treatment (median survival, 30.5 vs. 18.3 d, or a 66% improvement over control; $P = 0.0002$; Fig. S8).

Discussion

Delivery of Macromolecular Therapeutic Agents to the CNS. FUS can temporarily disrupt the BBB, increasing local EPR in the CNS. This technology is ideally suited for transcranial delivery of drugs with molecular weights greater than 400 Da (1, 14). However, although this technique works with substances with molecular weights as high as 150 kDa, penetration is still hampered at molecular weights of 2,000 kDa [approximately equivalent to 55 nm, as measured by TEM (15)].

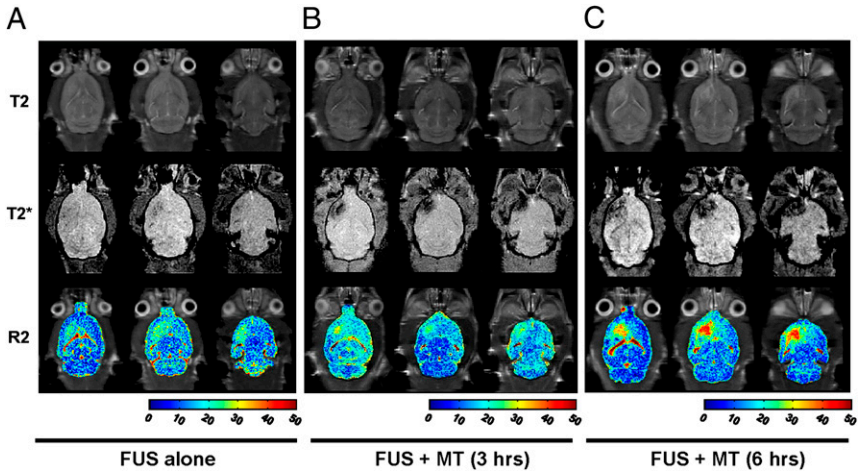

Fig. 3. In vivo imaging of MNP distribution in the brain (*Top*, T2-weighted images; *Middle*, T2*-weighted images; *Bottom*, combined R2 maps and T2-weighted images). (*A*) FUS sonication and MNP injection. (*B*) FUS followed by MT for 3 h after MNP injection. (*C*) FUS followed by MT for 6 h after MNP injection.

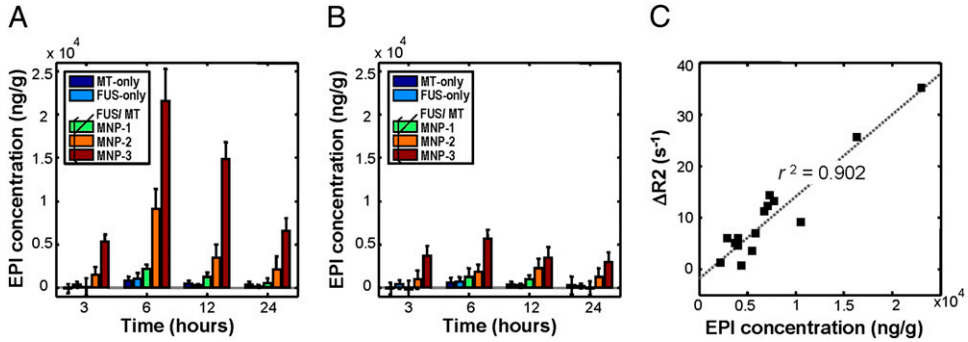

Fig. 4. Measurement of epirubicin accumulation in experimental animals over time. (*A* and *B*) Epirubicin concentration (μg of epirubicin/g tissue) in the experimental (*A*) and contralateral (*B*) brain hemispheres, respectively. MT-only, MT with MNP-3 (ie, without FUS); FUS-only, FUS with MNP-3 (ie, without MT); MNP-1–MNP-3, indicated MNPs administered in conjunction with combined FUS and MT. (*C*) Correlation between epirubicin concentration and the ΔR2 values (i.e., R2 values after subtraction of baseline values) as measured by MRI. Values are means ± SD (n = 3).

The current strategy to assess delivery of therapeutic substances [e.g., 50–150-kDa monoclonal antibodies (16) or <1-kDa chemotherapeutic agents (17)] involves their coadministration with a separate gadolinium type T1 contrast agent (<1 kDa). However, this technique estimates drug concentration indirectly, assuming a correlation between changes in image contrast and the concentration of the delivered substance. Also, conjugating small contrast agents (e.g., gadolinium) with therapeutic substances does not permit active targeting. However, an imaging probe that also has a therapeutic effect and/or target specificity must bind the agent to be delivered to the contrast agent, increasing the compound size and thus decreasing the likelihood that FUS will stimulate EPR. This study confirms that combining passive and active transport mechanisms can deliver large multifunctional molecules to the CNS. FUS treatment has been used safely to deliver 886 ± 327 ng doxorubicin per gram of tissue into normal brains (17). This is comparable to the levels of epirubicin delivered by FUS treatment alone in the present study (1,197 ± 226 ng/g and 1,162 ± 1,028 ng/g, as assessed by MRI and ICP-OES/HPLC detection, respectively). Doxorubicin delivery could be increased to 5,336 ± 659 ng/g (17), but at the expense of increased damage to brain tissue. In contrast, the approach used here synergistically combines FUS and MT to increase epirubicin delivery to the tumors by at least an order of magnitude (21,738 ± 3,477 ng/g and 22,070 ± 3,205 ng/g, as assessed by MRI and ICP-OES/HPLC detection, respectively) using a "safe" level of FUS exposure.

Use of R2 Maps and T2* Images to Detect MNPs. This study used T2*-weighted images and quantitative R2 maps to detect MNP accumulation in the brain in vivo. The T2*-weighted images showed increased sensitivity to the local field inhomogeneity induced by MNPs. Nonhomogeneous distribution or local accumulation of MNPs leads to an additional loss of phase coherence (i.e., dephasing) of the spins. This decreases the transverse relaxation times and thus contributes to a reduction in signal intensity (18), allowing such images to be used as a direct indicator of MNP distribution. It should be noted, however, that, although conceptually feasible, quantification of R2* (i.e., 1/T2*) is potentially nonreproducible because iron deposited over multiple sessions can produce strong magnetic field susceptibility, resulting in differences in field inhomogeneity (19). In contrast, R2 maps showed the high spin–spin relaxivity of MNPs, which was linear. The disadvantage of this approach is that multiple T2-weighted acquisitions at different echo times are required and comprehensive post-

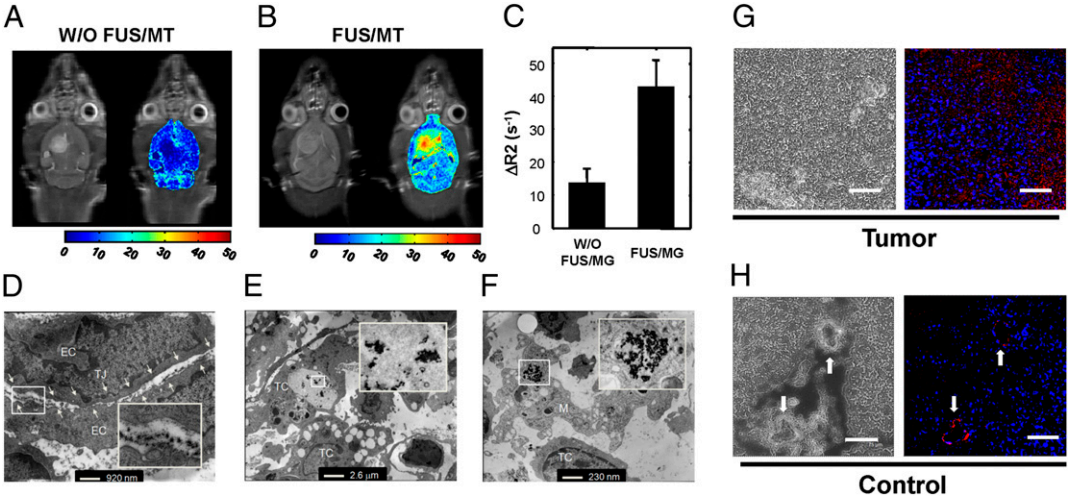

Fig. 5. In vivo T2-weighted MRI and the corresponding R2 maps of brain tumors without (*A*) or with (*B*) FUS and MT. (*C*) Measured relaxivities in tumor regions from the control and experimental groups. Values are means ± SD (n = 3). (*D–F*) TEM images of brain tumors show the presence of MNPs inside opened tight junction structures (TJ) and uptake by tumors cells (TC) and macrophages (M). Numerous caveolae in tumor cells or macrophages indicate apoptosis resulting from the uptake of epirubicin-MNPs. EC, endothelial cell. (*G* and *H*) Confocal micrographs of tissue from tumor and contralateral brain regions. Dark structures in the phase micrographs show MNPs (*Left*); fused fluorescence images (*Right*) indicate the presence of epirubicin (red) and DAPI-stained nuclei (blue). Arrows indicate the capillaries; epirubicin occurs in the capillary beds but does not penetrate into the brain parenchyma.

processing is necessary. Nevertheless, different information can be extracted from these two methods. For example, enhancements seen in T2*-weighted imaging contain higher spatial resolution and can show local concentration/aggregation of MNPs, whereas R2 maps provide a rather averaged MNP amount per unit volume. Thus, combining these techniques provides image resolution and quantitative information on MNP depositions.

Enhanced Drug Delivery to the BBB-Intact CNS. Most drugs used to treat CNS diseases that do not compromise the BBB (e.g., neurodegenerative diseases) must have sufficiently small molecular weights and need to be uncharged (or only partially ionized) at physiological pH to allow passive diffusion into brain. Increasing the lipid solubility of a drug to enhance BBB penetration can have undesirable effects such as decreasing overall solubility and/or bioavailability, increasing plasma protein binding, and increasing uptake by the liver or reticuloendothelial system.

Rather than designing therapeutic agents sufficiently small to penetrate the BBB, another approach is to temporarily open the BBB. Osmotically opening the barrier by infusing hypertonic mannitol through the carotid artery has been used successfully to treat human brain tumors (20, 21). Alternatively, bradykinin acting via B2 receptors in the luminal membrane of the endothelium can permeabilize the BBB, presumably by elevating intracellular free calcium levels and thus modulating tight junctions (22). Alkylglycerols administered via the carotid artery can also modulate the BBB (23). However, none of these approaches open the BBB locally, and this lack of selectivity can cause undesirable side effects in normal portions of the brain, as well as presenting systemic hazards (5). The use of noninvasive FUS to temporarily disrupt the BBB locally provides an ideal solution to the problems of drug design and localized delivery of such drugs to deep CNS tissues.

Enhanced Drug Delivery into Brain Tumors. Primary brain tumors or metastases to the brain from breast or lung cancers have markedly different vascular and hemodynamic characteristics than the intact brain (24–27). Vascular characteristics in tumors vary widely, and permeability does not necessarily correlate with tumor histology, size, or anatomical location. All these can restrict chemotherapeutic agents from reaching a therapeutic dose (28–30). Even small lipid-soluble agents such as 1–3-bis(2-chloroethyl)-1-nitrosourea, which in its natural form can penetrate the BBB, cannot accumulate in tumors (31). Low permeability and retention are even more pronounced in the case of large chemotherapeutic agents that cannot penetrate the BBB, such as lipid-encapsulated doxorubicin (17) or the epirubicin-MNPs used in the present study. Our results confirm that, by enhancing BBB permeability in tumors with FUS and concurrently applying MT, one can successfully deliver multifunctional macromolecules not only into brains with intact BBBs, but also to those in which the barrier has been compromised by pathological conditions, expanding the range of such molecules that could be used for integrated diagnostic and therapeutic treatments. Furthermore, the efficacy of such a treatment regimen has been confirmed experimentally (Fig. S8).

Potential Parameters for MT. Optimizing the specifications for MT can maximize active MNP delivery. The particles must be of a size sufficient to generate a strong enough magnetic moment such that, when the tumor (or the vascular system surrounding the tumor) is exposed to the magnetic field, the net attractive force acting on the MNPs can overcome the viscous drag and allow the particles to reach the targeted area. Active targeting can occur only when the MNPs are magnetized, and the efficiency of such magnetization varies with their crystalline structure, the process used to synthesize them, the material with which they are coated, and other factors, particularly size (32). For example, larger MNPs can induce thrombus in blood vessels more easily, whereas small MNPs (<100 nm) can be difficult to attract with low-strength magnetic fields, making size selection a dilemma. Previous studies showed that when a relatively strong magnetic field (>0.4 T) was applied, MNPs having high relaxivity (>40 $mM^{-1}s^{-1}$) could be used successfully for MT to superficial tissues (12, 33).

Although the present study demonstrates that MT can be used to deliver therapeutic drugs in small animal brains, it should be noted that the distance between the magnet pole and the animal brain was still short (<10 mm). Scaling up the current setup for clinical applications will still be challenging: The magnetic flux density from the single-pole magnet decayed sharply and was unable to provide effective MT in deep-seated tissues (Fig. S6). Possible improvements include increasing the magnet flux density by replacing the current permanent magnet with a superconducting electrical magnet coil, modifying the open-pole structure to a two-pole or closed-loop frame design (to reduce magnetic flux drop) (34), or designing MNPs with the use of highly magnetic materials (35).

Conclusions. This study provides an integrated nanomedicine platform to enhance and monitor delivery of multifunctional nanoparticles to the brain. FUS can locally and transiently disrupt the BBB, and the subsequent application of MT significantly improves deposition of therapeutic MNPs (at least an order of magnitude higher than previously reported approaches). The combined use of these techniques provides an important means to deliver therapeutic doses locally and simultaneously reduce the problem of systemic toxicity common to i.v.-administered therapeutic agents. More importantly, MNP distribution can be monitored by MRI, permitting quantification of drug delivery in real time in vivo.

Materials and Methods

Characterization of MNPs. A drop of diluted nanoparticle suspension was deposited on 300-mesh silicon-monoxide support films and dried under vacuum for 2 h. Images were acquired on a Phillips 400 transmission electron microscope operating at 100 kV. The superparamagnetic properties and magnetization of MNPs were measured using a superconducting quantum interference device (MPMS-7; Quantum Design). FT-IR spectra were acquired using a TENSOR 27 FT-IR spectrometer (Bruker) with a resolution of 4 cm. MNP samples were milled with KBr and pressed into a pellet for X-ray diffraction pattern analysis. Patterns were acquired from lyophilized samples with a D5005 X-ray diffractometer (Siemens) using Cu-Kα radiation (λ of 1.541Å) at 40 kV and 40 mA. Zeta potentials and hydrodynamic sizes were measured in water using a dynamic light scattering particle size analyzer (ZEN3600; Malvern). The polymers covering the MNPs were quantified by ICP-OES using a Varian 720-ES spectrometer. The relaxivities of the three MNPs generated for this study, as well as that of the commercially available carboxydextran-coated Resovist (60-nm hydrodynamic size; Schering), were measured in vitro in gel phantoms and in vivo. Standard samples of Poly[aniline-co-sodium N-(1-one-butyric acid) aniline]-coated MNPs (0–6.48 mmol/kg iron) were prepared as gel phantoms (1% gelatin) in 24-well plates. Standard R2 measurements were performed using a 3-T magnetic resonance imager (Trio with Tim, Magnetom; Siemens). The relaxivities reported are the means of five measurements.

Animal Preparation. All animal experiments were approved by the Institutional Animal Care and Use Committee of Chang Gung University and adhered to their experimental animal care guidelines. Thirty-nine normal rats (Sprague-Dawley, 300–400 g) were tested to confirm the efficacy of the proposed approach. Brain tumors were induced in another 14 rats by injection of cultured C6 tumor cells. Briefly, C6 tumor cells (10^6 cells/plate) were injected into the brains using a microdialysis pump system (CMA Microdialysis). Animals underwent FUS treatment on day 10 after tumor implantation to determine if the method could open an area of the BBB sufficiently large to cover the area of the induced tumors.

FUS Sonication. Before US treatment, animals were anesthetized by i.p. injection of chlorohydrate (30 mg/kg). The top of the cranium was shaved with clippers, and a PE-50 catheter was inserted into the jugular vein. The animal's head was attached tightly to a 4-cm^2 thin-film window directly under an acrylic water tank (Fig. S4 *A* and *B*). Cranial openings were filled with degassed water to serve as an acoustic coupling device. SonoVue SF6-coated US microbubbles (mean diameter 2–5 μm, 2.5 μg/kg; Bracco) were administered i.v. before treatment (with a time lapse <10 s). Each bolus injection

contained 0.1 mL microbubbles/kg body weight mixed with 0.2 mL of saline solution, followed by a 0.2-mL heparin flush.

Animal experiments were monitored using the 3-T magnetic resonance imager to localize the geometric center of the FUS and the energy exposure site (Fig. S4 *A* and *B*). US was delivered to the brain transcranially using a MR-compatible spherical transducer (diameter, 60 mm; radius of curvature, 80 mm; frequency, 400 kHz, electric-to-acoustic efficiency, 70%; Imasonics) with the center of the focal zone positioned at a penetration depth of 2 to 3 mm in each hemisphere. Single burst-mode US was delivered, with a burst length of 10 ms, a pulse-repetition frequency of 1 Hz, and total sonication duration of 120 s. For optimization studies, the input electric power used was 2 W, corresponding to an acoustic negative peak (i.e., spatial-peak, temporal-peak) pressure amplitude measured through the animal cranium equal to 0.62 MPa.

MT. Permanent magnets with peak magnetic flux densities of 0.2, 0.4, or 0.55 T were used to produce an inhomogeneous magnetic field. To concentrate the magnetic flux density onto the disrupted region of the BBB, the magnet was tilted at an angle to the brain (Fig. S4*C*), attached to the animal's scalp, and supported and tightened using a custom-made plastic belt for the desired duration (3–24 h). MRI images were acquired immediately after removal of the magnet.

MRI. Animals were assessed by MRI after US treatment and/or MT. All MRI images were acquired on a 3-T scanner using the standard wrist coil with an inner diameter of 13 cm. The animals were anesthetized with 2% isoflurane throughout the MRI imaging process, placed in an acrylic holder, and positioned in the center of the magnet. An i.v. bolus (0.1 mmol/kg) of gadopentetate dimeglumine MRI contrast agent (Magnevist; Berlex) was administered before scanning. To identify the region of the BBB disrupted by the FUS, contrast-enhanced T1 turbo spin-echo sequences were acquired using the following parameters: repetition/echo time, 780 ms/15 ms; slice thickness, 1.4 mm; matrix size, 128 × 256; field of view, 39 × 60 mm (resolution, 0.3 × 0.3 mm). T2-weighted images were obtained to produce R2 maps both in gel phantom or in vivo experiments by using a double-TE spin-echo sequence and acquired three times, using the following parameters: repetition time, 3,860 ms, echo time, 8/14, 28/57, and 85/228 ms; matrix, 128 × 256; field of view, 38 × 76 mm (resolution, 0.3 × 0.3 mm); and slice thickness, 1.4 mm. T2*-weighted images were used to observe the distribution of MNPs 3, 6, 12, and 24 h after MNP injection. T2-weighted imaging was also used to measure tumor volume.

Measurement of MNP and Epirubicin Deposition in Tissue. Animals were killed at 3, 6, 12, and 24 h after MNP injection. Brains were collected immediately, washed twice with normal saline solution, and dried under vacuum for 48 h at 80 °C. The dried samples were ground into powder, and the powders were acid-digested in 12 M aqua regia overnight. The iron content of the samples was measured by ICP-OES; each assay was performed in triplicate. Epirubicin concentration was calibrated by HPLC using a L-2400 UV detector and L-2130 pump (Hitachi) and a Supelcosil LC-18 column (4.6 × 250 mm). Each assay was performed in triplicate. The epirubicin concentration measured in tissues was 383 to 415 μg epirubicin/mg iron ion, with a consistent mean immobilization ratio of 395.6 ± 17.3 μg epirubicin/mg iron ion (Fig S9*C*). Thus, epirubicin concentration in tissues can be quantified reliably by measuring MNP concentration.

Histology and Microscopy. Evans blue was administered after FUS treatment to confirm BBB disruption (Fig. S4 *D* and *E*). Tissues were prepared after in vivo MRI analysis. Animals were killed 3, 6, 12, and 24 h after injection of dye and/or MNPs. Slides were stained with Prussian blue (Sigma) to detect iron deposited in cells/tissue samples. Briefly, brain sections mounted on slides were stained in a 1:1 mixture of 2% potassium ferrocyanide and 2% hydrochloric acid for 30 min at room temperature. The slides were rinsed with distilled water, counterstained with Nuclear Fast Red for 5 min, dehydrated, and photographed. Nuclei were stained with the fluorescent dye DAPI. Microscopic observations were performed using a Zeiss Axioplan imaging 2 microscope with AxioVision 4.1 imaging software, an AxioCam HRc camera, and Fluar 10×/0.50, Plan-Apochrome 20×/0.75, and Plan-Neofluar 100×/1.30 oil objectives (Carl Zeiss).

ACKNOWLEDGMENTS. This project was supported by National Science Council (Taiwan) Grants NSC-98-2221-E-182-045-MY3 and NSC-98-2218-E-182-008; Chang-Gung Memorial Hospital Grants CMRPD260042, CMRPD250013, and CMRPG350193; National Health Research Institute (Taiwan) Grant NHRI-EX95-9507NI; and Department of Health (Taiwan) Grant DOH98-TD-N-111-002.

1. Pardridge WM (2002) Drug and gene delivery to the brain: The vascular route. *Neuron* 36:555–558.
2. Begley D, Brightman MW (2003) *Peptide Transport and Delivery into the Central Nervous System*, eds Prokai L, Prokai-Tatrai K (Birkhäuser Verlag, Basel), pp 39–78.
3. Kreuter J (2001) Nanoparticulate systems for brain delivery of drugs. *Adv Drug Deliv Rev* 47:65–81.
4. Lockman PR, Mumper RJ, Khan MA, Allen DD (2002) Nanoparticle technology for drug delivery across the blood-brain barrier. *Drug Dev Ind Pharm* 28:1–13.
5. Hynynen K, et al. (2006) Focal disruption of the blood-brain barrier due to 260-kHz ultrasound bursts: a method for molecular imaging and targeted drug delivery. *J Neurosurg* 105:445–454.
6. Farokhzad OC, Langer R (2006) Nanomedicine: Developing smarter therapeutic and diagnostic modalities. *Adv Drug Deliv Rev* 58:1456–1459.
7. Sanvicens N, Marco MP (2008) Multifunctional nanoparticles—properties and prospects for their use in human medicine. *Trends Biotechnol* 26:425–433.
8. Veiseh O, Gunn JW, Zhang M (2010) Design and fabrication of magnetic nanoparticles for targeted drug delivery and imaging. *Adv Drug Deliv Rev* 62:284–304.
9. Sun C, Lee JSH, Zhang M (2008) Magnetic nanoparticles in MR imaging and drug delivery. *Adv Drug Deliv Rev* 60:1252–1265.
10. Torchilin VP (2006) Multifunctional nanocarriers. *Adv Drug Deliv Rev* 58:1532–1555.
11. Zimmer C, et al. (1997) Tumor cell endocytosis imaging facilitates delineation of the glioma-brain interface. *Exp Neurol* 143:61–69.
12. Chertok B, David AE, Huang Y, Yang VC (2007) Glioma selectivity of magnetically targeted nanoparticles: A role of abnormal tumor hydrodynamics. *J Control Release* 122:315–323.
13. Bigotte L, Olsson Y (1989) Distribution and toxic effects of intravenously injected epirubicin on the central nervous system of the mouse. *Brain* 112:457–469.
14. Muldoon LL, et al. (2007) Chemotherapy delivery issues in central nervous system malignancy: A reality check. *J Clin Oncol* 25:2295–2305.
15. Choi JJ, Wang S, Tung YS, Morrison B, 3rd, Konofagou EE (2010) Molecules of various pharmacologically-relevant sizes can cross the ultrasound-induced blood-brain barrier opening in vivo. *Ultrasound Med Biol* 36:58–67.
16. Kinoshita M, McDannold N, Jolesz FA, Hynynen K (2006) Noninvasive localized delivery of Herceptin to the mouse brain by MRI-guided focused ultrasound-induced blood-brain barrier disruption. *Proc Natl Acad Sci USA* 103:11719–11723.
17. Treat LH, et al. (2007) Targeted delivery of doxorubicin to the rat brain at therapeutic levels using MRI-guided focused ultrasound. *Int J Cancer* 121:901–907.
18. Corot C, Robert P, Idée J-M, Port M (2006) Recent advances in iron oxide nanocrystal technology for medical imaging. *Adv Drug Deliv Rev* 58:1471–1504.
19. Dahnke H, Schaeffter T (2005) Limits of detection of SPIO at 3.0 T using T2 relaxometry. *Magn Reson Med* 53:1202–1206.
20. Rapoport SI (2000) Osmotic opening of the blood-brain barrier: principles, mechanism, and therapeutic applications. *Cell Mol Neurobiol* 20:217–230.
21. Neuwelt EA, Barnett PA, Bigner DD, Frenkel EP (1982) Effects of adrenal cortical steroids and osmotic blood-brain barrier opening on methotrexate delivery to gliomas in the rodent: The factor of the blood-brain barrier. *Proc Natl Acad Sci USA* 79:4420–4423.
22. Emerich DF, Dean RL, Osborn C, Bartus RT (2001) The development of the bradykinin agonist labradimil as a means to increase the permeability of the blood-brain barrier: from concept to clinical evaluation. *Clin Pharmacokinet* 40:105–123.
23. Lee HJ, Zhang Y, Pardridge WM (2002) Blood-brain barrier disruption following the internal carotid arterial perfusion of alkyl glycerols. *J Drug Target* 10:463–467.
24. Groothuis DR, Fischer JM, Lapin G, Bigner DD, Vick NA (1982) Permeability of different experimental brain tumor models to horseradish peroxidase. *J Neuropathol Exp Neurol* 41:164–185.
25. Lesniak MS, Brem H (2004) Targeted therapy for brain tumours. *Nat Rev Drug Discov* 3:499–508.
26. Neuwelt EA, et al. (1985) Growth of human lung tumor in the brain of the nude rat as a model to evaluate antitumor agent delivery across the blood-brain barrier. *Cancer Res* 45:2827–2833.
27. Neuwelt EA, et al. (1986) Developments in the diagnosis and treatment of primary CNS lymphoma. A prospective series. *Cancer* 58:1609–1620.
28. Arosarena O, Guerin C, Brem H, Laterra J (1994) Endothelial differentiation in intracerebral and subcutaneous experimental gliomas. *Brain Res* 640:98–104.
29. Blasberg RG, et al. (1983) Regional blood flow in RT-9 brain tumors. *J Neurosurg* 58: 863–873.
30. Pathak AP, et al. (2001) MR-derived cerebral blood volume maps: issues regarding histological validation and assessment of tumor angiogenesis. *Magn Reson Med* 46: 735–747.
31. Liu H-L, et al. (2010) Blood-brain barrier disruption with focused ultrasound enhances delivery of chemotherapeutic drugs for glioblastoma treatment. *Radiology* 255: 415–425.
32. Goodwin S, Peterson C, Hoh C, Bittner C (1999) Targeting and retention of magnetic targeted carriers (MTCs) enhancing intra-arterial chemotherapy. *J Magn Magn Mater* 194:132–139.
33. Chertok B, et al. (2008) Iron oxide nanoparticles as a drug delivery vehicle for MRI monitored magnetic targeting of brain tumors. *Biomaterials* 29:487–496.
34. Dames P, et al. (2007) Targeted delivery of magnetic aerosol droplets to the lung. *Nat Nanotechnol* 2:495–499.
35. Lee H, Yoon T-J, Figueiredo J-L, Swirski FK, Weissleder R (2009) Rapid detection and profiling of cancer cells in fine-needle aspirates. *Proc Natl Acad Sci USA* 106: 12459–12464.